ADVANCED MATERIALS
www.advmat.de

Bi-Chiral Nanostructures Featuring Dynamic Optical Rotatory Dispersion for Polychromatic Light Multiplexing

Si-Jia Liu, Lin Zhu, Yi-Heng Zhang, Wen Chen, Dong Zhu, Peng Chen, and Yan-Qing Lu**

Chiral nanostructures featuring the unique optical activity have attracted broad interests from scientists. The typical polarization rotation of transmitted light is usually wavelength dependent, namely the optical rotatory dispersion. However, its dynamic tunability and intriguing collaboration with other optical degrees of freedom, especially the highly desired spatial phase, remain elusive. Herein, a bi-chiral liquid crystalline nanostructure is proposed to induce an effect called reflective optical rotatory dispersion. Thanks to the independent manipulation of opposite-handed self-assembled helices, spin-decoupled geometric phases are induced simultaneously. These naturally unite multi-dimensions of light and versatile stimuli-responsiveness of soft matter. Dynamic holography driven by heat and electric field is demonstrated with a fast response. For polychromatic light, the hybrid multiplexed holographic painting is exhibited with fruitful tunable colors. This study extends the ingenious construction of soft chiral superstructures, presents an open-ended strategy for on-demand light control, and enlightens advanced applications of display, optical computing, and communication.

1. Introduction

Chirality, as a ubiquitous wonder in nature ranging from DNA, plant cell walls, beetle exoskeletons to galaxies, keeps shedding light on research in physics, chemistry, and medicine.[1–3] Among diverse chiral structures, cholesteric liquid crystals (CLCs) have aroused extensive interests for their supramolecular chirality, fast self-assembly, and excellent flexibility, where liquid crystal (LC) molecules self-organize into 1D-photonic-crystal-like helices.[4,5] Such helical self-assembly naturally bridges the molecular and the wavelength scale, and also enables the distinctive spin-selective Bragg reflection.[6] Only the circular polarization with identical handedness to CLCs can be reflected within the photonic bandgap (PBG), which proves valuable in reflective displays,[7,8] color filters,[9] and mirrorless lasers.[10–12] Recently, the ever-progressing micro/nano-fabrication has further facilitated the sophisticated 3D management of CLC helices, bringing multifarious functionalities,[13,14] especially in the cutting-edge territory of light control.[15] Micro/nano CLC chiral structures have unlocked the capability of spin-selective and reflective geometric phase modulation.[16–18] Such optical elements manifest the merits of planar configuration, broadband operation and high efficiency, providing a competitive platform for beam steering, lensing, and processing.[19–21]

Harnessing multiple dimensions of light (e.g., amplitude, phase, polarization, and wavelength) plays a significant role in modern technology. It is universally recognized that the next generation of optical elements should all-roundly satisfy high efficiency, high compactness, multiple dimensions, and dynamic tunability. Metasurfaces, generally composed of metal/dielectric nanoscatterers, are considered a promising candidate.[22–24] They can concurrently manipulate numerous optical degrees of freedom in a typically static manner, while their dynamic functioning is a worthwhile but long-term task.[25–28] Fortunately, the emerging micro/nano-structured CLCs are definitely distinguished by excellent stimuli-responsiveness to heat,[16,29] electric field,[30–32] and light irradiation,[33–35] but the previously limited steerable dimensions strongly impede their potential. To overcome this, nature drops a hint at us by associating the polarization with the wavelength via optical rotatory dispersion in chiral media (see detailed introduction in Section S1, Supporting Information).[36] Aiming for on-demand light control, the ingenious collaboration with tunable spatial phase manipulation is highly desired, but still remains elusive.

In this study, we propose a preprogrammed bi-chiral CLC nanostructure for dynamic, polychromatic, and multiplexed light manipulation, and demonstrate it in the context of holography. Through the surface-initiated wash-out/refill process, CLCs with a right-handed polymer scaffold and a left-handed active layer are integrated into a single cell. This piecewise configuration brings about a dispersive polarization rotation named as the reflective optical rotatory dispersion (RORD), which is compatible with various functionalization methods. Through the precise and rewritable photoalignment, independent geometric phases can be encoded for left and right circular polarizations (LCP and RCP). For monochromatic light, smooth transformation from one image to another is yielded in response to polarizer rotation,

S.-J. Liu, L. Zhu, Y.-H. Zhang, W. Chen, D. Zhu, P. Chen, Y.-Q. Lu
National Laboratory of Solid State Microstructures
Key Laboratory of Intelligent Optical Sensing and Manipulation
College of Engineering and Applied Sciences, and Collaborative Innovation Center of Advanced Microstructures
Nanjing University
Nanjing 210093, China
E-mail: chenpeng@nju.edu.cn; yqlu@nju.edu.cn

The ORCID identification number(s) for the author(s) of this article can be found under https://doi.org/10.1002/adma.202301714

DOI: 10.1002/adma.202301714

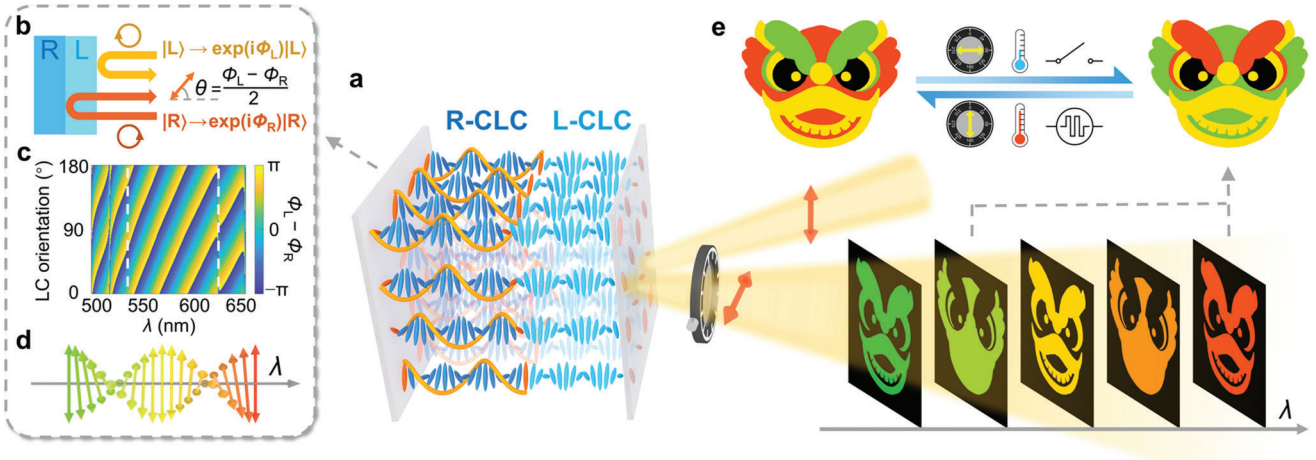

Figure 1. Schematic illustration of the dynamic polychromatic light multiplexing via bi-chiral self-assembled nanostructures. a) Wavelength-dependent reconstruction of target images from a bi-chiral CLC hologram. Light-blue and dark-blue rods represent L-CLC and R-CLC, respectively. Yellow springs surrounding the R-CLC represent the polymer scaffold. Double-ended orange arrows depict the polarizing and analyzing directions of the incident and reflected light, respectively. b) Spatially segregated reflection of LCP and RCP off the bi-chiral structure. c) The simulated dependence of the reflection phase difference between LCP and RCP on wavelengths and initial LC orientations (see detailed descriptions in the Experimental Section). d) The vivid illustration of the RORD phenomenon, where the reflected LP rotates along with the variant wavelength. e) Multicolored images of the "dancing lion" and their dynamic tunability via analyzer rotation, heat, or electric field control.

heat, or electric field. Particularly, the electrical response time can reach tens of microseconds. For polychromatic light, the hybrid multiplexed holography exhibits versatile coloring and dynamic switching. Our study unveils the unprecedented capabilities of chiral structures and opens new vistas for chiroptics.

2. Results and Discussion

2.1. Principle of Dynamic RORD and Spin-Decoupled Geometric Phase Modulation

Although natural structures usually prefer one certain chirality, we propose a bi-chiral architecture to further push the limits of chiroptics. As vividly shown in **Figure 1**a, the left-handed and right-handed CLCs (L-CLC and R-CLC) are spatially segregated in a single cell. The L-CLC sublayer, as an active layer, contains polymer-free LCs, while the R-CLC layer is stabilized by the polymer/LC nanocomposite. Corresponding unique characteristics are studied in the left block. Within the PBG from $n_o p$ to $n_e p$ (n_o/n_e denoting the ordinary/extraordinary refractive index of LCs and p the helical pitch), LCP and RCP components of the linearly polarized (LP) incident light can be respectively reflected by L-CLC and R-CLC at different surfaces (Figure 1b; Figure S1, Supporting Information), and derive the reflection phases of Φ_L and Φ_R. When the reflected LCP and RCP reconstitute the LP, its polarization angle θ typically differs from the incidence (assumed to be 0°), following:

$$\theta = \frac{\Phi_L - \Phi_R}{2} \tag{1}$$

Theoretically, the reflection phase difference between LCP and RCP can be expressed as

$$\Phi_L - \Phi_R = \Delta\Phi_P + \Delta\Phi_G = -\frac{4\pi}{\lambda} n_{eff} d - 2\alpha_L - 2\alpha_R + \Delta\Phi_0 \tag{2}$$

$\Delta\Phi_P$ and $\Delta\Phi_G$ represent the respective differences of propagation phases and geometric phases. λ is the incident wavelength, n_{eff} is the effective refractive index of L-CLC for the transmitted RCP, and d is the L-CLC thickness. α_L and α_R are the initial orientations on the incident side of L-CLC and R-CLC, and $\Delta\Phi_0$ is the extra phase difference. Accordingly, a wavelength dependence of $\Phi_L - \Phi_R$ occurs due to the propagation phase difference (Figure 1c; see details in Figure S2, Supporting Information), giving rise to the dispersive rotation of the reflected LP within PBG (Figure 1d). This phenomenon resembles the typical optical rotatory dispersion but stems from a different mechanism (see comparison in Section S1, Supporting Information), so we call it RORD. Meanwhile, the reflective geometric phases encoded into LCP and RCP light are $-2\alpha_L$ and $+2\alpha_R$, respectively, regardless of the wavelength.[15] They can be independently designed by programming different orientation patterns, which enables free vectorial light control. See detailed theoretical explanations in Section S2 (Supporting Information).

Based on the above principle, we employ such bi-chiral CLC to reconstruct a traditional Chinese "dancing lion", which features various colors and symbolizes safety and happiness. By designing spin-decoupled geometric phases, a vectorial hologram is encoded for an orthogonally LP dancing lion. The RORD effect establishes a one-to-many mapping between the reflected polarization and wavelengths, so the image filtered out by a fixed analyzer periodically varies with the wavelength (Figure 1a). With polychromatic light, color holography can be rationally expected by multiplexing two certain wavelengths (Figure 1e). Interestingly, $\Delta\Phi_P$ can be affected by multiple external fields, while $\Delta\Phi_G$ remains unchangeable. This enlightens versatile ways toward the dynamic regulation of RORD. Consequently, the reconstructed colors could be diversely tuned by polarizer rotation, heat or electric field (Figure 1e), predicting its great potential in dynamic and polychromatic light multiplexing.

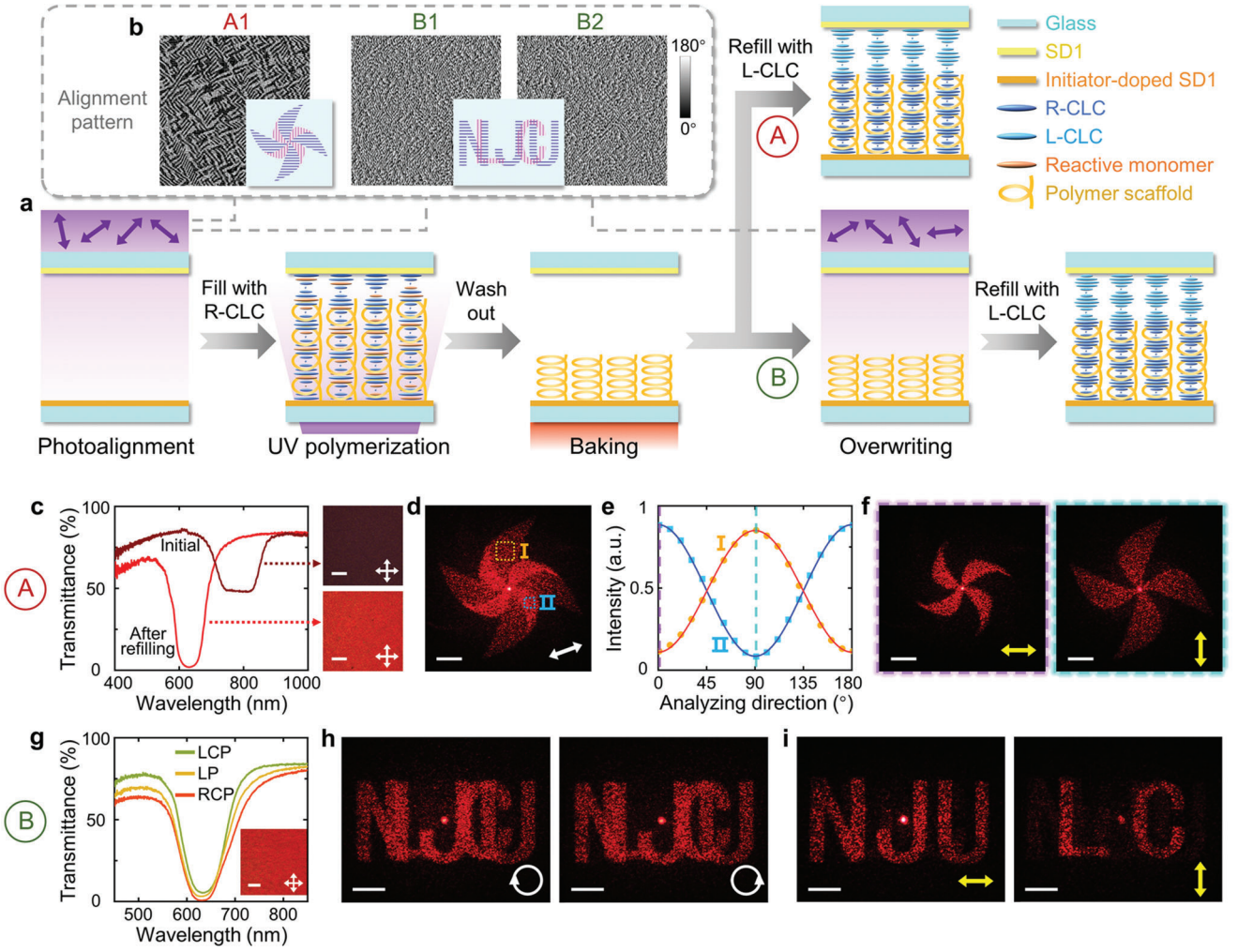

Figure 2. Design, fabrication, and characterization of the bi-chiral vectorial holograms. a) Fabrication process with two optional routes. Route B involves an additional overwriting process, which is omitted in route A. b) Alignment patterns of initial LCs designed for the target vectorial images. A1 is applied in route A, while B1 and B2 are applied, respectively, in the photoalignment and overwriting process in route B. c) Initial and final LP transmittance spectra of the pinwheel hologram fabricated through route A, and corresponding reflective polarized micrographs. Crossed white arrows depict the orthogonal polarizer and analyzer of the optical microscope. d) The vectorial pinwheel image reconstructed by LP incidence (white arrow). e) Relative intensities of region I and II marked in (d) under various analyzing directions. Dots and curves represent the measurements and fitting results, respectively. f) Polarization filtered images of (d) with horizontal/vertical analyzers (yellow arrows). g) LCP, LP, and RCP transmittance spectra of the letter hologram fabricated following route B. The inset is the polarized micrograph. h) Identical images generated by LCP (left) and RCP (right) light. i) Distinct images reconstructed with LP incidence and horizontal/vertical analyzers. Scale bars represent 200 μm in micrographs and represent 1 cm in reconstructed images.

2.2. PBG Engineering and Rewritable Photopatterning of Bi-Chiral Structures

To fabricate functional CLC nanostructures, we adopted a modified surface-initiated wash-out/refill process (**Figure 2**a). First, an empty cell coated with the photoalignment agent SD1 was exposed to LP UV light for photopatterning, reorienting the SD1 molecules perpendicular to the UV polarization.[15] The Gerchberg–Saxton algorithm[37] was employed to design the alignment patterns (Figure 2b), by which a polarization-multiplexed hologram was encoded (see detailed derivation in Section S3 and Figures S3 and S4, Supporting Information). After filling the cell with R-CLC (the E7/RM257/R5011 mixture), the mixture self-assembled into helical superstructures with the directing of SD1, thus the geometric phase for RCP was successfully imprinted. Then, the cell was polymerized by UV light from the photoinitiator-doped substrate. Through surface-initiated photopolymerization, the reaction initially proceeds from the initiator-doped side, thus forming the surface-tethered polymer scaffold (see relevant characterizations in Figure S5, Supporting Information).[29,38] Next, by immersing the cell in acetone, nonreactive molecules and unreacted monomers were washed out, leaving the shrunk and porous scaffold. A follow-up baking was adopted to conduct the PBG engineering. The baking temperature and duration would influence the swelling ability of the scaffold, determining the ultimate PBG of the R-CLC layer.

Finally, the cell was refilled with certain L-CLC (the E7/S5011 mixture) for the overlapped PBG. Upon refilling, LC molecules quickly entered the nanopores within the polymer scaffold, causing the surface-tethered scaffold to swell a lot, but still far from the other substrate. Since the right-handed and photopatterned helical polymer template overpowers the nascent left-handed preference of the refilled L-CLC mixture,[38] the scaffold preserved both the right-handed chirality and the initial orientations (Figure S6, Supporting Information), forming the well-patterned R-CLC layer and reflecting RCP light.[39,40] The extra space was full of the refilled L-CLC, and thick enough to highly reflect the LCP light. Interestingly, the L-CLC layer was anchored by the initiator-free substrate, which could be optionally overwritten thanks to the erasability of SD1. Without overwriting (route A in Figure 2a), the consistent surface alignment would induce spin-coupled conjugated geometric phases for LCP and RCP, just like those classic conditions. If the overwriting process was carried out through differently polarized UV exposure (route B in Figure 2a), the original alignment pattern would be entirely replaced by a new one, imprinting a distinct phase for LCP. Such sophisticated bi-chiral structures enable spin-decoupled geometric phase modulation with hyper-reflection, significantly breaking the limits of conventional LCs.

2.3. On-Demand Vectorial Holography

As the simplest example, the holographic reconstruction of a centrosymmetric vectorial image, a "pinwheel", is presented in Figure 2c–f. The corresponding alignment pattern (A1 in Figure 2b) was imprinted following route A. The initial PBG of the bi-chiral hologram is centered at 784 nm before polymerization (Figure 2c), transmitting ≈50% of the LP incident light. After refilling, the hologram attains an overlapped PBG for LCP and RCP. The LP transmittance approaches zero in the shared PBG centered at 631 nm (Figure 2c), indicating the hyper-reflection. Such PBG change is also confirmed by the variant structural colors at different fabrication stages (Figure 2c; Figure S7a,b, Supporting Information). When illuminating the initiator-free side of the hologram with a LP He-Ne laser, the reconstructed vectorial pinwheel is shown in Figure 2d (see the cases of LCP and RCP incidence in Figure S7c, Supporting Information). According to the design, region I (big vanes) and II (small vanes) should be orthogonally polarized. Figure 2e depicts their relative intensities with the rotation of an analyzer, which fit well with the Malus' law. When analyzed horizontally, a small pinwheel is clearly observed. While vertically analyzed, a distinct big pinwheel is attained with a high contrast ratio (Figure 2f). As for a 45° analyzer, there exist both big and small vanes (Figure S7d, Supporting Information).

Breaking the geometric phase conjugation and thus the centrosymmetric reconstruction between LCP and RCP remains challenging for traditional LC devices. Fortunately, this can be overcome by the proposed rewritable photopatterning in route B (B1 and B2 in Figure 2b). The fabricated letter hologram possesses a nearly overlapped PBG (centered at 631 nm), and properly exhibits the red structural color (Figure 2g). With the illumination of LCP or RCP, the superposition of "NJU" and "LC" can be observed (Figure 2h). Notably, the central symmetry between these two images has been thoroughly broken. As for LP incidence, a vectorial image is expected with space-variant polarizations (Figure S8a, Supporting Information). When analyzed horizontally, the pure image of "NJU" is clearly obtained, while only "LC" is observed with a vertical analyzer (Figure 2i). These verify that either centrosymmetric or asymmetric images can be encoded into orthogonal polarization channels.

2.4. Dynamic Holography Based on Multi-Stimuli Responsive RORD

Benefiting from the rich stimuli-responsiveness of CLC superstructures, dynamic light control can be expected. We first explore the thermal tunability of the aforementioned letter hologram. For LCP incident light, its temperature-dependent transmittance spectra are shown in **Figure 3**a, where the PBG blue-shifts and narrows upon heating. The observed PBG blue-shift is mainly caused by the spring-like pitch compression of the L-CLC layer with p reducing and also slightly affected by the refractive index change, while the PBG narrowing is mainly attributed to the thermally increased n_o and reduced n_e within L-CLC.[41] For RCP incidence, thermo-induced PBG narrowing is also observed (Figure S8b, Supporting Information). Since here L-CLC is polymer-free and the L-CLC layer is designed to be several times thinner than the R-CLC layer, the LCP spectral shift with temperature is relatively larger. Such responsiveness is verified by the varying structural color from red (30 °C) to orange (50 °C) (Figure 3a). At 55 °C, the dark red color appears with halved reflectance owing to the chiral nematic-isotropic phase transition of L-CLC (see corresponding spectra in Figure S8c,d, Supporting Information).

Owing to these variable nanostructures and refractive indices, $\Phi_L - \Phi_R$ changes with temperature as well, resulting in the intriguing thermo-controlled RORD. As a proof, the co-polarized reflectance spectra of a uniformly aligned sample are measured at 30 and 50 °C with the setup in Figure 3b. The obtained two spectra (Figure 3c) both rise and fall periodically within the PBG, matching well with the RORD effect (see simulation results in Figure S9, Supporting Information). For each spectrum, two narrow peaks appear at the wavelengths where the reflected LP is parallel to the polarizer, while the valleys appear at the wavelengths where the reflected LP is perpendicular to the polarizer. From 30 to 50 °C, the peaks/valleys in the two spectra are approximately opposite to each other, indicating that a global polarization rotation of ≈90° is induced upon heating. Therefore, for the hologram with a fixed vertical analyzer, the "LC" image at 30 °C can gradually transform into a pure "NJU" image with the increasing temperature (Figure 3d; see intermediate states in Figure S8e, Supporting Information). The transformation from "NJU" to "LC" is also observed in the cooling process, proving the good reversibility.

Electrical tuning is more favorable for its fast response and good reliability. Here, polymer-dispersed L-CLCs are introduced to stabilize the hologram texture (see detailed measurements in Figure S10a,b, Supporting Information). As illustrated in Figure 3e, in the active L-CLC layer, some LC molecules are confined in the nanopores distributed across the polymer network. Their electrically-induced reorientation will change n_{eff},

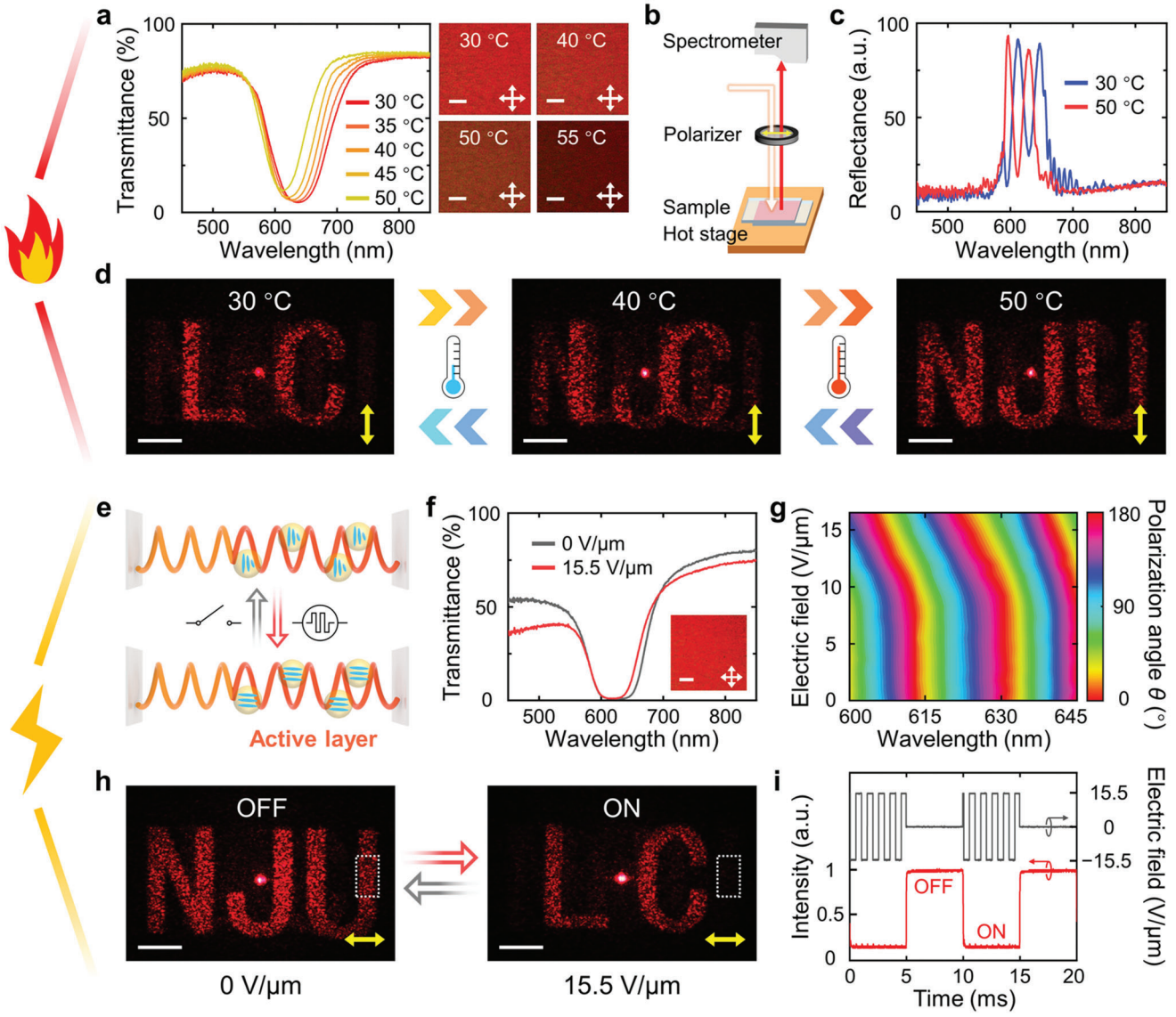

Figure 3. Thermally and electrically tunable holography via functional bi-chiral nanostructures. a) LCP transmittance spectra and polarized micrographs of the thermally tunable hologram at different temperatures. b) The optical setup to measure the temperature-dependent polarized reflectance spectra in (c). d) Reversible thermal switching of the reconstructed image with a fixed vertical analyzer (yellow arrows). e) Schematic illustration of the electrical tuning mechanism. Orange and yellow springs represent the polymerized L-CLC and R-CLC, respectively. Blue rods in the spheres refer to LC molecules in the nanopores across the L-CLC polymer network. f) LCP transmittance spectra of the electrically tunable hologram under different electric field. The inset is the polarized micrograph at 0 V μm^{-1}. g) The dependence of the reflected polarization angle on the wavelength and applied electric field. h) Reversible electrical switching of the reconstructed image with a fixed horizontal analyzer. i) The applied amplitude-modulated 1 kHz square wave (upper) and corresponding electrical response curve (lower) for the intensity of white dotted region in (h). Scale bars represent 200 μm in micrographs and represent 1 cm in reconstructed images.

thus altering $\Phi_L - \Phi_R$ and the RORD effect. In the experiment, Figure 3f presents the LCP transmittance spectra with/without electric field. When a 15.5 V μm^{-1} electric field is applied, the short-wavelength edge of the PBG persists that is different from the thermal response, while the long-wavelength edge blue-shifts, proving the invariant n_o and the reduced n_e of L-CLC. Such spectral change is highly consistent with that of the electrically-induced reorientation of active LC molecules in polymer-dispersed CLCs.[30,31] As for RCP, since the dense polymer networks in the R-CLC layer strongly hinder the reorientation of LC molecules under electric field, there exhibits no obvious change within PBG (Figure S10c, Supporting Information).

With adequate thickness of the L-CLC layer and proper electric field, the dynamic control of the global polarization rotation can reach 90° for wavelengths within PBG. Figure 3g shows the dependence of the reflected polarization angle θ on the wavelength and electric field. Owing to the RORD effect, θ changes with the wavelength regardless of the electric field. As for a specific wavelength, θ changes rapidly after exceeding the electric field threshold (≈9 V μm^{-1}, i.e., ≈135 V for the used 15-μm-thick cell), and

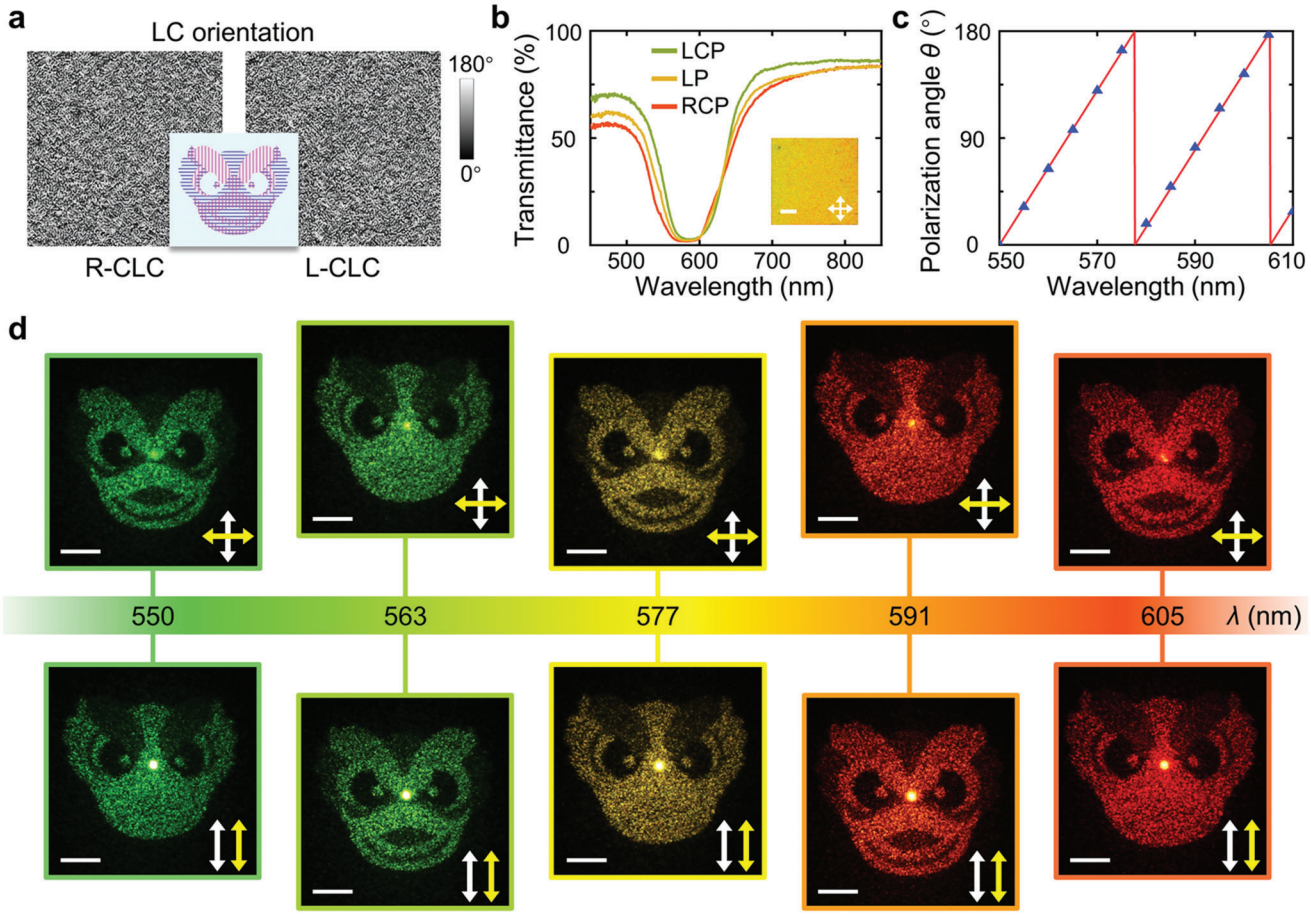

Figure 4. Hybrid multiplexed polychromatic holography. a) LC orientation distributions designed for a vectorial "dancing lion". b) LCP, LP, and RCP transmittance spectra and the polarized micrograph of the fabricated bi-chiral hologram. c) The wavelength dependence of the reflected polarization angle. Blue dots represent the experimental measurements and are fitted with a red sawtooth line. d) Various images reconstructed with orthogonal/parallel polarizers at five specific wavelengths. White and yellow arrows depict the polarizing and analyzing directions, respectively. Scale bars represent 200 μm in the micrograph and represent 1 cm in reconstructed images.

a variation of ≈90° could be achieved at 15.5 V μm^{-1}. When the bi-chiral hologram is illuminated by LP light, the vectorial superposition of "LC" and "NJU" is reconstructed (Figure S10d, Supporting Information). With a horizontal analyzer, the "NJU" image is thoroughly filtered out at 0 V μm^{-1} (OFF state). When switching to 15.5 V μm^{-1} (ON state), due to the electrically tunable RORD, "NJU" disappears immediately, and "LC" takes the place (Figure 3h). The switching from "LC" to "NJU" is also realized with a vertical analyzer and various applied voltages (Figure S10e, Supporting Information).

Moreover, the electrical switching time is measured by recording the intensity change (90% to 10%, or 10% to 90%) in certain diffraction regions (e.g., the white dotted region in Figure 3h) with a highly time-resolved photodetector when applying an amplitude-modulated 1 kHz square wave (Figure 3i). The obtained switching-on and switching-off time are as short as 44 and 36 μs, respectively (see detailed acquisition in Figure S11, Supporting Information). Such response speed is approximately two orders of magnitude faster than common LC devices, which is attributed to the electrical response of LC molecules in nanopores in such a polymer/CLC nanocomposite system.[30] This indicates a modulation rate over 12 kHz, promoting fast and time-division-multiplexed light manipulation.

2.5. Color-Tunable Holographic Painting

The RORD effect bridges the polarization and the wavelength, thus opening up a new avenue for polychromatic multiplexed holography. Here, a new bi-chiral hologram is customized for a vectorial "dancing lion" by imprinting different orientation patterns in L-CLC and R-CLC (**Figure 4**a). Fabricated through route B, this hologram finally exhibits a yellow structural color with hyper-reflection (Figure 4b; see more measurements in Figure S12a,b, Supporting Information). The overlapped PBG ranges from 546 to 635 nm approximately, covering the colors from green to red. Illuminated with polychromatic LP light, θ changes almost linearly with the wavelength, and rotates by 360° within the 55 nm range (Figure 4c), agreeing well with the simulation in Figure S2e, Supporting Information. With an orthogonal or parallel analyzer, the reconstructed image varies periodically with the wavelength (Figure 4d). For example, the images at 550, 577, and

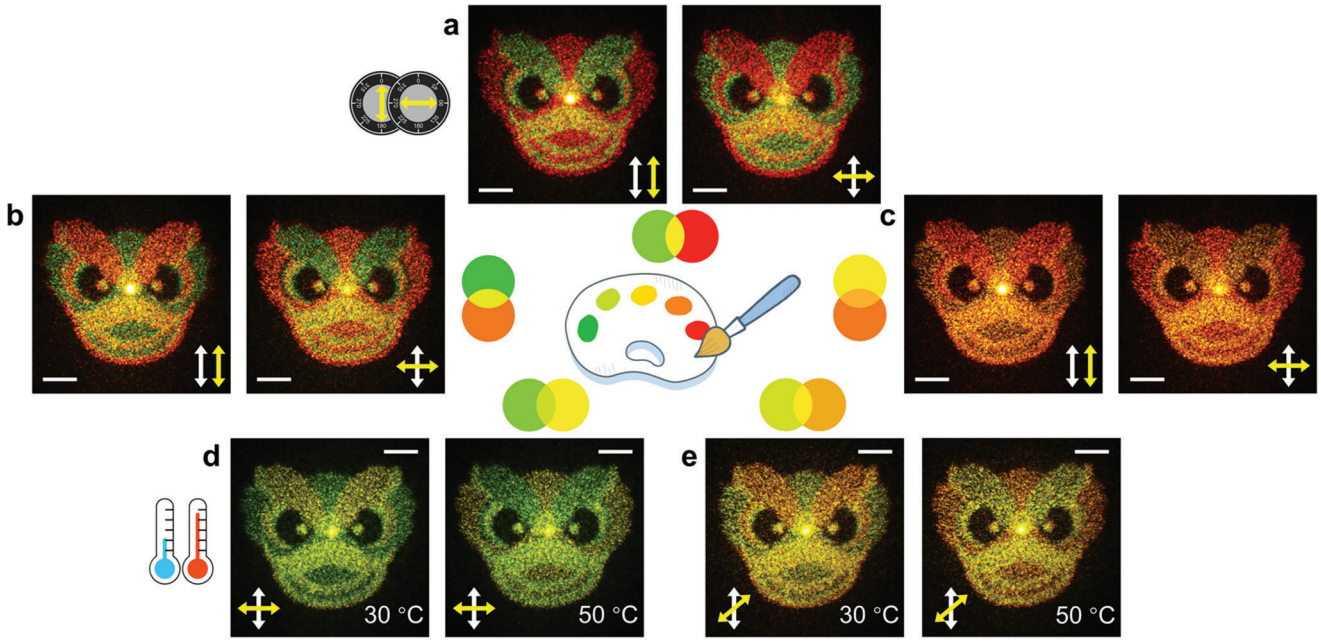

Figure 5. Color-tunable holographic painting of dancing lions. Multicolored dancing lions constructed by multiplexing the wavelengths of a) 563 and 605 nm, b) 550 and 591 nm, and c) 577 and 591 nm. Thermo-controlled coloring of the dancing lions by mixing d) 563 nm with 577 nm, and e) 569 nm with 583 nm at different temperatures. The angles between the incident vertical LP (white arrows) and different analyzing directions (yellow arrows) are 0°/90° in (a–c), 90° in (d), and 53° in (e). Scale bars represent 1 cm in all reconstructed images.

605 nm are almost the same except for the dispersive projection angle. Meanwhile, for the same analyzer, a distinct image can be obtained at 563 and 591 nm, showing negligible cross talk from the other channel.

Accordingly, the color-tunable holographic painting can be achieved with concurrent illumination of multiple wavelengths (**Figure 5**). With LP incidence at 563 and 605 nm, the dancing lion is colored green, red, and the mixed color yellow (Figure 5a). The green/red regions can gradually turn into red/green, respectively, by rotating the analyzer (Movie S1, Supporting Information). Besides, multicolored dancing lions mixing green with orange (550 and 591 nm) and yellow with orange (577 and 591 nm) are also finely reconstructed (Figure 5b,c), exhibiting the polarization-dependent dynamic coloring.

To make the dancing lions active without any mechanical operation, the aforementioned thermo-tunable RORD is introduced. With a fixed orthogonal analyzer, a dancing lion mixing green with yellow (563 and 577 nm) is generated at 30 °C (Figure 5d). As the temperature rises to 50 °C, green exchanges with yellow, leading to a distinct colorful image (see more examples in Figure S12c,d, Supporting Information). Theoretically, abundant unlisted wavelengths and other analyzing directions can be further exploited to create infinite multicolored paintings. An example of mixing 569 nm with 583 nm is shown in Figure 5e with a 37° analyzer.

3. Conclusion

Typically, the optical rotatory dispersion in chiral media is uniform and fixed. Its dynamic combination with spatial phase control is almost unachievable in traditional systems and first explored in this study. The proposed bi-chiral nanostructures offer a fantastic platform, facilitating the dynamic, polychromatic, and multi-dimensional light engineering. Owing to the hyper-reflection within PBG and pure phase modulation, a high efficiency up to ≈66% can be reached. The transmittance loss outside the PBG is mainly due to the Fresnel reflection at the air-glass substrate interfaces and the scattering induced by the complex polymer networks. In addition to heat and electric field, RORD may also be facilely controlled by mechanical stress,[42] light irradiation,[43] and other stimuli, paving the way for extensive future researches. On the other hand, the external field could be sensed smartly through the varying reconstructed image. For richer functionality, the rewritability of the proposed device can be further exploited through extending it to a second wash, photoalignment and refill process (see experimental demonstration in Figure S13, Supporting Information). For higher capacity, different transverse regions in the bi-chiral CLC can be rationally segmented for separate PBGs, establishing additional wavelength channels.[7] More independent polarization channels might also be induced via introducing engineered noise.[44] As for cases where stability rather than tunability is the premier requirement, the self-standing all-polymer configuration can be adopted.[45]

In summary, a new strategy for dynamic light multiplexing is proposed via functional bi-chiral nanostructures. Through the surface-initiated wash-out/refill process, stimuli-responsive CLCs with opposite chirality could piecewise coexist, triggering the dynamically tunable RORD effect. On-demand vectorial holography is realized featuring satisfactory switchability, with a fast response down to 36 μs. For polychromatic light, the dynamic color holography is demonstrated through the hybrid multiplex-

ing of polarizations and wavelengths. This study extremely extends the construction of soft chiral nanostructures and enriches the concept of chiroptics. Since high efficiency, high compactness, multi-dimensions, and dynamic tunability have been satisfied simultaneously, the advanced display, high-security encryption, and multiplexed communication might be expected.

4. Experimental Section

Liquid Crystal Materials: The sulfonic azo-dye SD1 (DIC, Japan) was dissolved in dimethylformamide at a concentration of 0.35 wt.%. The photoinitiator-doped SD1 was prepared by mixing the SD1 solution with 0.15 wt.% diphenyl ketone. The initial R-CLC mixture contains nematic LC E7 (HCCH, China), right-handed chiral dopant R5011 (HCCH, China), and LC reactive monomer RM257 (HCCH, China) at a weight ratio of 78.1:1.9:20 for the pinwheel and thermally tunable holograms, 78.9:1.1:20 for the electrically tunable hologram, and 78:2:20 for the color hologram. The different concentrations of R5011 determine the initial PBG positions of R-CLC. The refilled L-CLC contains E7 and left-handed chiral dopant S5011 (HCCH, China) at a weight ratio of 97.6:2.4 for the pinwheel and thermally tunable holograms, and 97.4:2.6 for the color hologram. The different concentrations of S5011 determine the ultimate PBG of L-CLC, which is expected to overlap with that of the ultimate R-CLC. The L-CLC refilling the electrically tunable sample contains E7, RM257, diphenyl ketone and S5011 at a weight ratio of 81.8:15:0.8:2.4. This specific concentration of RM257 was picked out after attempts of various concentrations to form the proper polymer-dispersed L-CLC layer. See chemical structures of SD1, diphenyl ketone, RM257 and R5011/S5011 in Figure S14 (Supporting Information).

Sample Fabrication: Indium-tin-oxide glass substrates after UV-Ozone cleaning were spin-coated with SD1 or photoinitiator-doped SD1 solution. After curing at 100 °C for 10 min, a substrate with the photoinitiator-doped alignment layer was assembled with another photoinitiator-free substrate through spreading the 15-µm spacer/glue mixture on the upper and lower edges of one substrate. When the glue was dried, the 15-µm-thick cell was formed. Then, the surface-initiated wash-out/refill process was implemented (Figure 2a). To imprint the designed LC orientation patterns, UV photoalignment and the optional overwriting were carried out through a multistep partly overlapping exposure process with the digital-micromirror-device-based photopatterning system.[15] The filling/refilling process was conducted at 72 °C through the left and right unsealed edges of the cell. In the polymerization process, the cell was exposed to non-polarized UV light (365 nm, 4.6 mW cm^{-2}) for 15 min from the photoinitiator-doped side. After immersed in acetone for 12 h to fully wash out the nonreactive molecules, in order to engineer the final spin-selective PBG, the shrunk scaffold was baked at 100 °C for 8 min for the pinwheel and color holograms, at 100 °C for 6 min for the thermally tunable hologram, and at 140 °C for 20 min for the electrically tunable hologram. The higher baking temperature and longer baking time led to the weaker swelling ability of the R-CLC polymer scaffold, which means larger space can be spared for the refilled L-CLC. After refilling, the electrically tunable sample was further illuminated by UV light (365 nm, 4.6 mW cm^{-2}) for 10 min from the initiator-free side, in order to form the polymer-dispersed L-CLC.

Numerical Calculations: The reflection field of the bi-chiral CLC structure was calculated with Berreman's 4 × 4 matrix algorithm.[46] The specific simulation conditions are present in Figure S2a,b (Supporting Information). Figure 1c illustrates the simulated dependence of the reflection phase difference between LCP and RCP ($\Phi_L - \Phi_R$) on wavelengths and initial LC orientations. With a fixed LC orientation, $\Phi_L - \Phi_R$ changes regularly with the wavelength in PBG, leading to the RORD effect. As for a fixed wavelength, $\Phi_L - \Phi_R$ varies linearly with the initial LC orientation, which is ascribed to the CLC geometric phase. Some other simulation results are shown in Figure S2c–f (Supporting Information) and explained in detail in Section S2 (Supporting Information). All numerical results highly accord with Equation (2).

Characterizations: All data were measured at room temperature unless a specific temperature is marked. All micrographs were captured by a polarized optical microscope (Ci-POL, Nikon, Japan) with crossed polarizer and analyzer under the reflective mode. All transmittance and reflectance spectra were measured by a spectrometer (PG2000-Pro-EX, Ideaoptics, China) with a halogen light source (iDH2000H-HP, Ideaoptics, China). For experiments in Figures 2 and 3, the incident light came from a He-Ne laser (HNL020L, Thorlabs, USA), while the experiments in Figures 4 and 5 utilized a supercontinuum fiber laser (SuperK EVO, NKT Photonics, Denmark) filtered at different wavelengths by a multichannel acousto-optic tunable filter (SuperK SELECT, NKT Photonics, Denmark). The incident polarization was controlled by a polarizer and a quarter-wave plate, and the reflected light was optionally filtered with an analyzer. The reconstructed images were projected to a black screen at a distance of 50 cm and captured by a visible digital camera (EOS M100, Canon, Japan). The captured colors and pattern changes of reconstructed images are quite close to what is seen with the naked eye. The intensity of light was detected by a digital optical power meter (PM100D, Thorlabs, USA), and the conversion efficiency was defined as the power ratio of the far-field image excluding the central light spot to the total reflectance. Temperature control was conducted by a transparent hot stage (ET-TY115, Etool Technology, China). The driving electric field was generated by a waveform generator (33500B, Keysight Technologies, USA) and amplified by a high-voltage amplifier (2350, TEGAM, USA). The electrical response curve was measured by a photodetector (PDA100A-EC, Thorlabs, USA) and an oscilloscope (MDO34, Tektronix, USA).

Supporting Information

Supporting Information is available from the Wiley Online Library or from the author.

Acknowledgements

S.-J.L. and L.Z. contributed equally to this work. This work was supported by the National Key R&D Program of China (nos. 2021YFA1202000 and 2022YFA1405000), the National Natural Science Foundation of China (NSFC) (nos. 62222507, 62175101, and 12004175), the Innovation Program for Quantum Science and Technology (no. 2021ZD0301500), and the Natural Science Foundation of Jiangsu Province (nos. BK20212004 and BK20200311).

Conflict of Interest

The authors declare no conflict of interest.

Data Availability Statement

The data that support the findings of this study are available from the corresponding author upon reasonable request.

Keywords

chiral nanostructures, dynamic holography, geometric phases, light multiplexing, liquid crystals

Received: February 22, 2023
Revised: April 14, 2023
Published online: June 29, 2023

[1] V. Sharma, M. Crne, J. O. Park, M. Srinivasarao, *Science* **2009**, *325*, 449.
[2] A. Scarangella, V. Soldan, M. Mitov, *Nat. Commun.* **2020**, *11*, 4108.
[3] Y. Chang, R. Middleton, Y. Ogawa, T. Gregory, L. M. Steiner, A. Kovalev, R. H. N. Karanja, P. J. Rudall, B. J. Glover, S. N. Gorb, S. Vignolini, *Proc. Natl. Acad. Sci. U.S.A.* **2021**, *118*, e2111723118.
[4] H. K. Bisoyi, Q. Li, *Chem. Rev.* **2022**, *122*, 4887.
[5] S.-U. Kim, Y.-J. Lee, J. Liu, D. S. Kim, H. Wang, S. Yang, *Nat. Mater.* **2022**, *21*, 41.
[6] M. Faryad, A. Lakhtakia, *Adv. Opt. Photonics* **2014**, *6*, 225.
[7] X. Zhan, F.-F. Xu, Z. Zhou, Y. Yan, J. Yao, Y. S. Zhao, *Adv. Mater.* **2021**, *33*, 2104418.
[8] L. Qin, X. Liu, K. He, G. Yu, H. Yuan, M. Xu, F. Li, Y. Yu, *Nat. Commun.* **2021**, *12*, 699.
[9] W. Park, H. Park, Y. S. Choi, D. K. Yoon, *Adv. Opt. Mater.* **2022**, *10*, 2201099.
[10] H. Coles, S. Morris, *Nat. Photonics* **2010**, *4*, 676.
[11] J. Xiang, A. Varanytsia, F. Minkowski, D. A. Paterson, J. M. D. Storey, C. T. Imrie, O. D. Lavrentovich, P. Palffy-Muhoray, *Proc. Natl. Acad. Sci. U.S.A.* **2016**, *113*, 12925.
[12] F. F. Xu, Y. J. Li, Y. Lv, H. Dong, X. Lin, K. Wang, J. Yao, Y. S. Zhao, *CCS Chem.* **2020**, *2*, 369.
[13] T. Orlova, F. Lancia, C. Loussert, S. Iamsaard, N. Katsonis, E. Brasselet, *Nat. Nanotechnol.* **2018**, *13*, 304.
[14] A. J. J. Kragt, D. C. Hoekstra, S. Stallinga, D. J. Broer, A. P. H. J. Schenning, *Adv. Mater.* **2019**, *31*, 1903120.
[15] P. Chen, B.-Y. Wei, W. Hu, Y.-Q. Lu, *Adv. Mater.* **2020**, *32*, 1903665.
[16] J. Kobashi, H. Yoshida, M. Ozaki, *Nat. Photonics* **2016**, *10*, 389.
[17] R. Barboza, U. Bortolozzo, M. G. Clerc, S. Residori, *Phys. Rev. Lett.* **2016**, *117*, 053903.
[18] M. Rafayelyan, E. Brasselet, *Phys. Rev. Lett.* **2018**, *120*, 213903.
[19] P. Chen, L.-L. Ma, W. Duan, J. Chen, S.-J. Ge, Z.-H. Zhu, M.-J. Tang, R. Xu, W. Gao, T. Li, W. Hu, Y.-Q. Lu, *Adv. Mater.* **2018**, *30*, 1705865.
[20] J. Xiong, Q. Yang, Y. Li, S.-T. Wu, *Light Sci. Appl.* **2022**, *11*, 54.
[21] P. Chen, L.-L. Ma, W. Hu, Z.-X. Shen, H. K. Bisoyi, S.-B. Wu, S.-J. Ge, Q. Li, Y.-Q. Lu, *Nat. Commun.* **2019**, *10*, 2518.
[22] A. Arbabi, Y. Horie, M. Bagheri, A. Faraon, *Nat. Nanotechnol.* **2015**, *10*, 937.
[23] C.-W. Qiu, T. Zhang, G. Hu, Y. Kivshar, *Nano Lett.* **2021**, *21*, 5461.
[24] N. A. Rubin, A. Zaidi, A. H. Dorrah, Z. Shi, F. Capasso, *Sci. Adv.* **2021**, *7*, eabg7488.
[25] S.-Q. Li, X. Xu, R. M. Veetil, V. Valuckas, R. Paniagua-Domínguez, A. I. Kuznetsov, *Science* **2019**, *364*, 1087.
[26] T. Cui, B. Bai, H. B. Sun, *Adv. Funct. Mater.* **2019**, *29*, 1806692.
[27] H. Ren, X. Fang, J. Jang, J. Bürger, J. Rho, S. A. Maier, *Nat. Nanotechnol.* **2020**, *15*, 948.
[28] H. Gao, Y. Wang, X. Fan, B. Jiao, T. Li, C. Shang, C. Zeng, L. Deng, W. Xiong, J. Xia, M. Hong, *Sci. Adv.* **2020**, *6*, eaba8595.
[29] M. E. McConney, V. P. Tondiglia, J. M. Hurtubise, L. V. Natarajan, T. J. White, T. J. Bunning, *Adv. Mater.* **2011**, *23*, 1453.
[30] Y. Inoue, H. Yoshida, H. Kubo, M. Ozaki, *Adv. Opt. Mater.* **2013**, *1*, 256.
[31] S. M. Wood, J. A. J. Fells, S. J. Elston, S. M. Morris, *Macromolecules* **2016**, *49*, 8643.
[32] B. Liu, C.-L. Yuan, H.-L. Hu, H. Wang, Y.-W. Zhu, P.-Z. Sun, Z.-Y. Li, Z.-G. Zheng, Q. Li, *Nat. Commun.* **2022**, *13*, 2712.
[33] Z.-G. Zheng, Y. Li, H. K. Bisoyi, L. Wang, T. J. Bunning, Q. Li, *Nature* **2016**, *531*, 352.
[34] P. Chen, Z. X. Shen, C. T. Xu, Y. H. Zhang, S. J. Ge, L. L. Ma, W. Hu, Y. Q. Lu, *Laser Photonics Rev.* **2022**, *16*, 2200011.
[35] R. Lan, J. Bao, R. Huang, Z. Wang, L. Zhang, C. Shen, Q. Wang, H. Yang, *Adv. Mater.* **2022**, *34*, 2109800.
[36] C.-W. Chen, I. C. Khoo, *Proc. Natl. Acad. Sci. U.S.A.* **2021**, *118*, e2021304118.
[37] R. W. Gerchberg, W. O. Saxton, *Optik* **1972**, *35*, 237.
[38] M. E. McConney, V. P. Tondiglia, J. M. Hurtubise, T. J. White, T. J. Bunning, *Chem. Commun.* **2011**, *47*, 505.
[39] L. Zhu, C.-T. Xu, P. Chen, Y.-H. Zhang, S.-J. Liu, Q.-M. Chen, S.-J. Ge, W. Hu, Y.-Q. Lu, *Light Sci Appl* **2022**, *11*, 135.
[40] C. T. Xu, P. Chen, Y. H. Zhang, X. Y. Fan, Y. Q. Lu, W. Hu, *Appl. Phys. Lett.* **2021**, *118*, 151102.
[41] Y. Li, Y. J. Liu, H. T. Dai, X. H. Zhang, D. Luo, X. W. Sun, *J. Mater. Chem. C* **2017**, *5*, 10828.
[42] Y. Geng, R. Kizhakidathazhath, J. P. F. Lagerwall, *Nat. Mater.* **2022**, *21*, 1441.
[43] Z. Zheng, H. Hu, Z. Zhang, B. Liu, M. Li, D.-H. Qu, H. Tian, W.-H. Zhu, B. L. Feringa, *Nat. Photonics* **2022**, *16*, 226.
[44] B. Xiong, Y. Liu, Y. Xu, L. Deng, C.-W. Chen, J.-N. Wang, R. Peng, Y. Lai, Y. Liu, M. Wang, *Science* **2023**, *379*, 294.
[45] T. J. White, D. J. Broer, *Nat. Mater.* **2015**, *14*, 1087.
[46] D. W. Berreman, T. J. Scheffer, *Phys. Rev. Lett.* **1970**, *25*, 577.